Research Article | Vol. 29, No. 2 / 18 January 2021 / Optics Express 2780

Optics EXPRESS

Experimental analysis of the measurement precision of spectral water-leaving radiance in different water types

JIANWEI WEI,[1,2,*] MENGHUA WANG,[1] ZHONGPING LEE,[3] MICHAEL ONDRUSEK,[1] SHUAI ZHANG,[3] AND SHERWIN LADNER[4]

[1] NOAA Center for Satellite Applications and Research, 5830 University Research Ct., College Park, MD 20740, USA
[2] Global Science & Technology Inc., 7501 Greenway Center Dr., Suite 1100, Greenbelt, MD 20770, USA
[3] University of Massachusetts Boston, 100 Morrissey Blvd, Boston, MA 02125, USA
[4] Naval Research Laboratory, 1009 Balch Blvd., Stennis Space Center, MS 39529, USA
[*] jianwei.wei@noaa.gov

Abstract: The on-water radiometric approach employs a unique provision to obtain water-leaving radiance from nadir ($L_w(\lambda)$) which can be used for the calibration of ocean color satellites. In this effort, we address the measurement precision associated with $L_w(\lambda)$ from a single on-water instrument, which is an important aspect of measurement uncertainty. First, we estimated the precision as the ratio of the standard deviation of the means of repeated measurements to the mean of these measurements. We show that the measurement precision for $L_w(\lambda)$ is within 2.7–3.7% over 360–700 nm. The corresponding remote sensing reflectance spectra ($R_{rs}(\lambda)$) from the same instrument also exhibit a high precision of 1.9–2.8% in the same spectral domain. These measured precisions of radiance and reflectance over the 360–700 nm range are independent of the optical water type. Second, we quantified the consistency of on-water $L_w(\lambda)$ and $R_{rs}(\lambda)$ from two collocated systems for further insight into their measurement repeatability. The comparison reveals that $L_w(\lambda)$ measurements in the 360–700 nm agree with each other with an absolute percentage difference of less than 3.5%. The corresponding $R_{rs}(\lambda)$ data pairs are subjected to increased differences of up to 8.5%, partly due to variable irradiance measurements ($E_s(\lambda)$). The evaluation of measurement precision corroborates the reliability of the on-water acquisition of radiometric data for supporting satellite calibration and validation.

1. Introduction

The radiometric objective of satellite observations is to achieve normalized water-leaving radiance ($nL_w(\lambda)$, wavelength dependence suppressed hereafter) or remote sensing reflectance R_{rs} under 5% uncertainty at the blue band in open oceans [1–3]. Toward this radiometric goal, the satellite sensors must have an on-orbit vicarious calibration (gains) applied which are derived from pristine/non-contaminated in situ and satellite matchups [4–7]. This process requires that the ground-truth nL_w and R_{rs} be measured with uncertainty on the order of 1–2%, or what is referred to more generally as "1% radiometry" [8].

The ocean radiometric products in field measurements are usually obtained with two sampling strategies: above- and in-water radiometry. Each approach is characteristic of a unique way of determining L_w, which is the fundamental quantity in ocean color remote sensing. The above-water approach measures the total radiance originating from the sea surface along sensor-zenith angle (θ_v) and sensor-azimuth angle (φ_v), $L_t(\theta_v,\varphi_v)$, and the incoming sky radiance, $L_{sky}(180°-\theta_v,\varphi_v)$. L_w can then be determined with the following measurement equation

$$L_w = [L_t(\theta_v, \varphi_v) - \rho L_{sky}(180°-\theta_v, \varphi_v)]C_{RQ}C_{f/Q}, \tag{1}$$

#413784 https://doi.org/10.1364/OE.413784
Journal © 2021 Received 30 Oct 2020; revised 22 Dec 2020; accepted 24 Dec 2020; published 15 Jan 2021

where ρ is the sea surface reflectance, a function of the viewing direction, solar-zenith angle (θ_s), wind speed, and wavelength [9,10]. C_{RQ} and $C_{f/Q}$ are coefficients introduced to remove the dependence from the viewing geometry and the bidirectional effects [11]. For an in-water approach, the upwelling radiance along water depth z, denoted as $L_u(z)$, is often measured from more than half a meter below the surface to greater than ~10 m or tens of meters in depth. Then the depth profile of $L_u(z)$ is extrapolated back to just below the water surface to obtain $L_u(0^-)$ with the estimated diffuse attenuation coefficient for this radiance (K_L). Finally, $L_u(0^-)$ can be transmitted across the air-water interface to achieve L_w. Thus, the in-water measurement equation for L_w can be expressed as

$$L_w = \frac{t}{n^2} L_u(z) \exp[zK_L] \frac{1}{1-\varepsilon}, \tag{2}$$

where t/n^2 is the transmittance of $L_u(0^-)$ and is treated as a constant of 0.54 [12]; the spectral dependence of t/n^2 is reportedly within 1% in visible bands [13]. In Eq. (2), ε refers to the self-shading error, which is a function of θ_s and water inherent optical properties (IOPs) [14]. The above- and in-water radiometry have been extensively tested, amended, and reviewed [11,15–18]. To date, both schemes have been widely used in the ocean color community. Long-term calibration platforms have also been established, including the Marine Optical Buoy (MOBY) [19], the buoy used for the acquisition of long-term optical time series (BOUSSOLE) [20], and the Aerosol Robotic Network – Ocean Color (AERONET-OC) [11].

The on-water radiometry is an addition to the collection of satellite ocean optical calibration and validation protocols [21,22] and has recently received more attention [23]. Different from the above- and in-water methods, the on-water approach determines L_w by employing a provision to prevent the skylight and sunlight from interfering with the measurements [22,24] while eliminating additional corrections and uncertainty for this contamination. The on-water L_w product can be derived with the following measurement equation

$$L_w = L_w{}' \frac{1}{1-\varepsilon}, \tag{3}$$

where $L_w{}'$ is the measured water-leaving radiance, which is uncorrected for the self-shading error. A number of recent studies have demonstrated the applications of the on-water radiometric products with persuasive results [12,25–29].

A growing body of literature on analyses of in situ radiance and reflectance uncertainties has developed based on the in- and above-water measurements. Measurements with the smallest uncertainties were reported in the ocean subtropical waters. At the MOBY site, for instance, where the chlorophyll-a (CHL) concentration is about 0.07 mg m^{-3}, the spectrally averaged (400–600 nm) difference between independent in-water L_w measurements and MOBY data is about 3.1% [30]. In turbid coastal waters, the radiometric uncertainties can increase to a more noticeable level. In this regard, Zibordi et al. [31] conducted multiple optical experiments in the Adriatic Sea (CHL = 0.6–1.5 mg m^{-3}) and found that the spectrally averaged differences of L_w measurements from multiple platforms are generally within ~5–7%, while differences for R_{rs} vary between ~6% and 9%. Multiple factors may have contributed to these uncertainty results, including calibration, processing, instrument difference, and environmental disturbance, etc. In fact, the uncertainties of the satellite R_{rs} product also vary with water types [32], with smaller values for the open ocean and much higher values in coastal waters. Estimation of the field measurement uncertainties demands characterization of not only the measurement accuracy but also measurement precision, and ideally, their potential dependence on water types. Currently, there is a lack of uncertainty estimates of on-water radiance and reflectance measurements.

In this study, we evaluate one aspect of the measurement uncertainty of L_w and R_{rs}, i.e., measurement precision. We focus on the on-water hyperspectral radiometric measurements. Specifically, this contribution is composed of two major efforts: i) assessment of the measurement

Optics EXPRESS

precision of L_w and R_{rs} in different types of waters, and ii) quantification of the consistency of in situ radiometric measurements determined by collocated on-water instruments. We report that the water-leaving radiance and remote sensing reflectance spectra can be obtained from the on-water observations with high precision from 360 nm to 700 nm.

2. Classification of optical water types

We first describe the classification scheme used to sort the radiometric data into different optical water types (OWTs). The method was developed earlier by Wei et al. [33], which divides the global waters into about two dozen OWTs (see Fig. 1(a)). Each OWT is characteristic of a normalized remote sensing reflectance, defined as

$$nR_{rs}(\lambda_i) = \frac{R_{rs}(\lambda_i)}{\sqrt{\sum R_{rs}(\lambda_j)^2}}. \tag{4}$$

In the current study, λ_i refers to a total of five nominal center wavelengths at 412, 443, 488, 551, and 670 nm [34]. OWT 1 represents the "clearest" oceanic waters, where R_{rs} decreases predictably with the increase of the wavelength. From OWTs 1 to 23, generally speaking, waters experience a decrease in the R_{rs} blue-green band ratios, $R_{rs}(443)/R_{rs}(551)$. In other words, the ranking of OWTs 1–23 is in connection with their ocean biological status, such as CHL and the absorption coefficient of phytoplankton, a_{ph}.

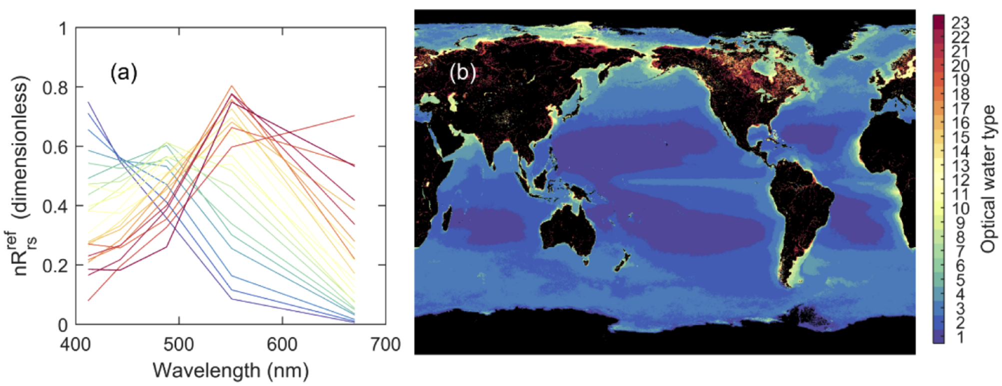

Fig. 1. (a) Normalized remote sensing reflectance spectra at five nominal bands of 412, 443, 488, 551, and 670 nm for classification of optical water types (replotted after Wei et al. [33] and Wei et al. [34]) and (b) example distribution of the optical water types in the global ocean derived from the climatology of VIIRS R_{rs} data.

Taking the above spectra as references, one can sort any given R_{rs} spectrum into a specific water type with the following steps. First, we calculate the cosine distances between the test R_{rs} spectrum and each of the reference spectra as

$$d = 1 - \frac{\sum [nR_{rs}^{ref}(\lambda_i) \cdot R_{rs}(\lambda_i)]}{\sqrt{\sum [nR_{rs}^{ref}(\lambda_i)]^2 \sum [R_{rs}(\lambda_i)]^2}}, \; i = 1, 2, \ldots 5, \tag{5}$$

where nR_{rs}^{ref} is the reference spectra given in Fig. 1(a). Second, the minimal d is identified from Eq. (5) and the occurrence number of the minimal d is regarded as the water type for the R_{rs} spectrum.

Figure 1(b) gives an example of the optical water types derived for the global ocean. This map is based on climatology (2003–2018) of R_{rs} data from the Visible Infrared Imaging Radiometer

Suite (VIIRS) onboard the Suomi National Polar-orbiting Partnership (SNPP) satellite. It is clear that the vast open oceans involve a handful of water types (approximately varying from OWTs 1 to 6). In particular, OWT 1 is coincident with the five subtropical gyres. From OWTs 1 to 6, the ratios of $R_{rs}(443)/R_{rs}(551)$ gradually decrease, implicating increase of CHL and a_{ph}. The OWTs 7–23 are present in coastal and inland waters.

3. Radiometric data and analyses

3.1. Description of field measurements

We conducted the on-water radiometric measurements during multiple cruises along the U.S. coastal ocean (Fig. 2). The sampling areas included MOBY (Lanai, Hawaii), the northern Gulf of Mexico, the South-Atlantic Bight, the Mid-Atlantic Bight, and Massachusetts Bay to the southwest of the Gulf of Maine. Successful deployments were retrieved at 232 stations, representative of multiple optical water types, ranging from OWTs 1 to 22. Table 1 summarizes the water bio-optical properties and atmospheric conditions for all experiments. Among all measurements, the MOBY data represent clear subtropical gyre waters. The IOPs, including the sum of the absorption coefficient of particles and colored dissolved organic matter (CDOM), $a_{pg}(443)$, and the particle backscattering coefficient, $b_{bp}(443)$, are small with their median values equal to 0.016 m^{-1} and 0.0014 m^{-1}, respectively. The most turbid waters were sampled in the northern Gulf of Mexico, where the median values of $a_{pg}(443)$, $b_{bp}(443)$, and CHL are approximately 0.50 m^{-1}, 0.028 m^{-1}, and 4.9 mg m^{-3}, respectively. The atmospheric conditions involved clear, overcast, and mixed sky with scattered clouds. The solar-zenith angles are moderate, varying between 30°–55°. The seas ranged from very calm situations to waves of ~1 m high.

Table 1. A summary of the on-water radiometric measurements and corresponding environmental conditions. The light absorption of particles, CDOM, and particulate backscattering coefficients were estimated using the inversion algorithm of Lee, et al. [37]. CHL concentrations of surface waters were determined with the high-performance liquid chromatography (HPLC) approach.

	Gulf of Mexico	Hawaii	Massachusetts Bay	South Atlantic Bight	Mid-Atlantic Bight
Year	2013	2014	2013-2017	2014-2018	2019
N	66	19	76	67	23
Sky condition	variable	variable	mostly clear	variable	mostly sunny
θ_s, Deg.	24–87 (48) [a]	27–42 (30)	25–85 (43)	11–83 (55)	34–69 (53)
$a_{pg}(443)$, m^{-1}	0.023–1.66 (0.50)	0.016–0.018 (0.016)	0.12–0.46 (0.15)	0.027–0.68 (0.10)	0.012-0.35 (0.072)
$b_{bp}(443)$, m^{-1}	0.0016–0.20 (0.028)	0.0013–0.0015 (0.0014)	0.0018-0.033 (0.0026)	0.0009–0.51 (0.0044)	0.0013–0.015 (0.0021)
CHL, mg m^{-3}	0.14–52 (4.9)	0.06–0.10 (0.07) [b]	0.15–9.1 (1.2)	0.22–6.1 (0.59)	0.045–5.1 (0.27)
OWTs	2–5,7,9–10, 12,14–18, 21–22	1	7, 10, 14	3,4,7,9,11,12,15,17	1-5,9,12,15

[a] The value in parentheses represents the median of the corresponding quantity.
[b] Estimations from VIIRS.

An on-water radiometric system was deployed at each station to obtain L_w and the above-water downwelling irradiance (E_s) data. Briefly, the on-water instrument was built on an in situ free-fall profiling unit, known as the hyperspectral profiler or HyperPro (s/n: MPR-184; University of Massachusetts Boston (UMB)) from Satlantic. It has a floating collar (40 cm in diameter) installed around the electronic hub, onto which two fins with extended arms are attached. Two hyperspectral radiometers (HyperOCR, 350–800 nm, spectral increment of 3.3 nm) for L_w and E_s

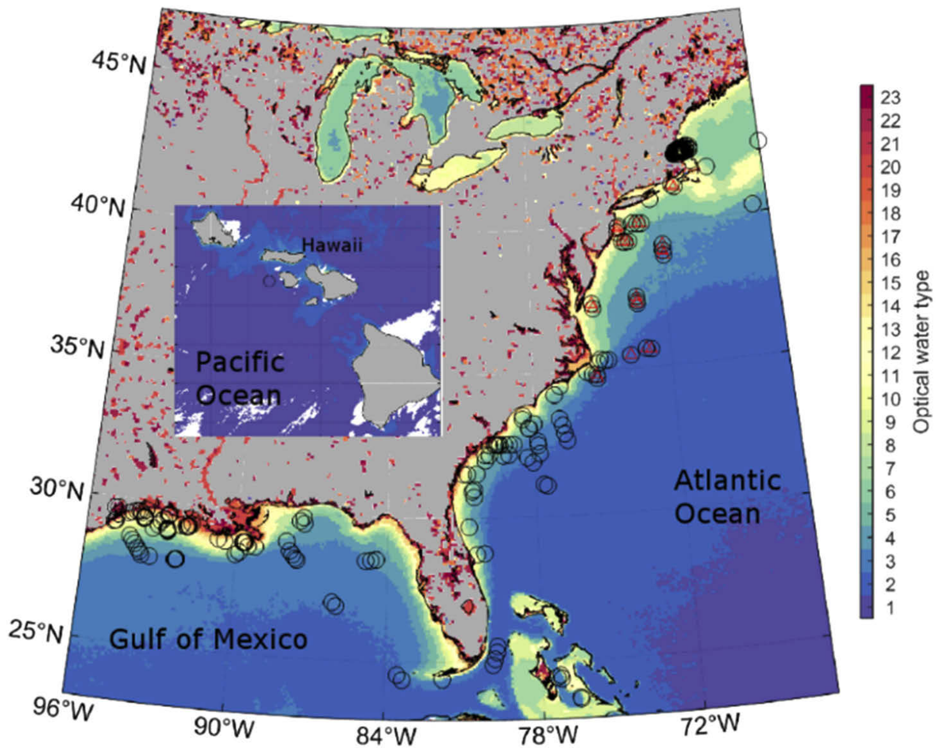

Fig. 2. Station map of in situ radiometric measurements in the U.S. coastal ocean. The insert shows the location of MOBY next to Lanai, Hawaii. The open circles ("○") and triangles ("Δ") refer to stations used for estimation of the relative uncertainty and for intercomparison analysis, respectively. The OWTs in background are derived from the climatology of NOAA VIIRS R_{rs} product (9 km).

are placed vertically at each end of the two extension arms. The irradiance sensor faces upward, while the radiance sensor looks downward. Further, a customized black cone (with a diameter of the bottom opening of 10.5 cm; known as the skylight-blocking apparatus) is connected to the end of the radiance sensor. The whole system is balanced with payloads such that the bottom edge of the cone is only slightly (by a few centimeters) immersed in the water. The skylight-blocking apparatus (i.e., cone) effectively blocks skylight and sunlight contamination reflected from above the sea surface from entering the fore optics of the sensor. As such, the signals recorded by the radiance sensor represent the actual radiance emerging from underneath the water surface.

During field experiments, the instrument package was released from the stern and was kept over ~30 m away from the ship before sampling. During sampling, the radiance sensor was always operating at the side facing the Sun, thereby minimizing the potential shadowing effect from the float [35]. At each station, we continuously logged the radiance and irradiance data for about 5–10 minutes. As a result, thousands of radiance and irradiance spectra were recovered from each deployment and were available for post-processing for subsequent uncertainty analysis. Details on the instrumental configuration and deployment can be found in the previous reports [12,22,23,26].

All radiometers used in this study were frequently calibrated following the standard ocean color protocols [36]. No significant radiometric drift or bias was observed.

3.2. Estimation of uncertainties

We estimated the measurement precision for L_w and R_{rs} from continuously recorded telemetry data, with the following steps:

(i) *Pre-processing*

We used the manufacturer-provided data analysis software PROSOFT to convert the raw telemetry data to Level-2 data. The products at this level include radiometrically calibrated radiance and irradiance, after applying the absolute and dark correction coefficients. The calibrated radiance and irradiance data were then interpolated onto a constant wavelength interval and common time coordinate. A threshold of instrument tilt (5°) was applied to discard those radiance and irradiance data beyond this threshold. This procedure results in a time series of instantaneous $L_w{}'(t)$ and $E_s(t)$, where t is the observation time. The ratio of $L_w{}'(t)$ to $E_s(t)$ is regarded in this study as the instantaneous remote sensing reflectance, $R_{rs}{}'(t)$,

$$R_{rs}{}'(t) = \frac{L_w{}'(t)}{E_s(t)}. \tag{6}$$

(ii) *Quality control of $L_w{}'(t)$ measurements*

Quality control was performed to identify and remove potentially contaminated radiance measurements. For this task, we used $R_{rs}{}'(t)$ data, instead of $L_w{}'(t)$ or $E_s(t)$ data, for subsequent data filtering, inasmuch as $R_{rs}{}'(t)$ are generally insensitive to the change of sky radiance distribution [38]. We first estimated the probability density function (PDF) for $R_{rs}{}'(t)$ based on the data at 698 nm, using a MATLAB function called *ksdensity*. From the PDF, the first mode of the distribution function was located. Then $R_{rs}{}'(t)$ spectra (and corresponding $L_w{}'(t)$ and $E_s(t)$ data) were filtered out if $R_{rs}{}'(t)$ values at 698 nm were beyond ±15% of the first mode. After this filtering, the remaining data still consist of a sufficiently large number of individual $L_w{}'(t)$ and $E_s(t)$ spectra.

(iii) *Mean spectra of repeated measurements*

We split up $L_w{}'(t)$ data into sequential segments to simulate repeated measurements of the "same" water parcels. Each data sequence, $L_{w,i}{}'(t)$, with the sequence number i varying from 1 to 10, retains roughly the same number of observations, and is determined from the actual data points available. A median radiance spectrum, $\bar{L}'_{w,i}$, was then derived for each $L_{w,i}{}'(t)$. In parallel, the same procedure of segmentation and averaging was also applied to $R_{rs,i}{}'(t)$ to derive a median spectrum, $\bar{R}'_{rs,i}$.

(iv) *Correction for self-shading error*

The self-shading error was modeled as a function of diffuse attenuation coefficient of waters (K), instrument radius (r), and solar-zenith angle right below water surface (θ_w) [35], with

$$\varepsilon_i = 1 - \exp\left[-K\frac{r}{\tan\theta_w}\right], \tag{7}$$

where K is further estimated as a function of the absorption coefficient (a) and backscattering coefficient (b_b),

$$K = (3.15\sin\theta_w + 1.15)\exp(-1.57b_b)a + (5.62\sin\theta_w - 0.23)\exp(-0.5a)b_b. \tag{8}$$

Then, a spectral optimization procedure was evoked to search for ε_i with $\bar{R}'_{rs,i}$ as the input.

Optics EXPRESS

Finally, the shade-corrected radiance for i^{th} sequence, $\bar{L}_{w,i}$, was derived as

$$\bar{L}_{w,i} = \bar{L}'_{w,i} \frac{1}{1-\varepsilon_i}. \tag{9}$$

The shade-corrected $\bar{R}_{rs,i}$ was determined in a similar process to Eq. (9).

(v) Constraining the variability of incident irradiance

Note that the ambient light field usually is not constant or stable during the observation of radiance and irradiance. Thus, the variation of the light field will affect the uncertainty estimates for L_w. To reduce such influence, we use the coefficient of variation (CV, the ratio of standard deviation to the mean) of 10% of $E_s(551)$ as a constraint. When the E_s data exceeded this constraint, all associated radiance measurements were excluded from subsequent uncertainty analysis for L_w. However, we did not apply this constraint for R_{rs} uncertainty analysis, considering that R_{rs} is generally insensitive to the variation of irradiance.

(vi) *Quantification of measurement precision*

In this context, the measurement precision is defined as the ratio of the standard deviation (STD) of the mean of repeated measurement results to the mean of these measurements. We first calculated STD of these $\bar{L}_{w,i}$ spectra as,

$$\sigma_{Lw} = \sqrt{\frac{1}{N-1}\sum_{i=1}^{N}(\bar{L}_{w,i} - \bar{L}_w)^2}, \tag{10}$$

where $\bar{L}_w$ corresponds to the mean of all $\bar{L}_{w,i}$ spectra and N is the total number of segments. The measurement precision of the water-leaving radiance at the nadir was then determined as,

$$U_{Lw} = \frac{\sigma_{Lw}}{\bar{L}_w} \times 100\%. \tag{11}$$

Similarly, the measurement precision of R_{rs} was retrieved as the following

$$U_{Rrs} = \frac{\sigma_{Rrs}}{\bar{R}_{rs}} \times 100\%, \tag{12}$$

where σ_{Rrs} and $\bar{R}_{rs}$ are STD and mean of all $\bar{R}_{rs,i}$ data, respectively.

3.3. Intercomparison of collocated measurements

For insight into the repeatability of on-water observations, we conducted an intercomparison analysis of collocated measurements from two identical instruments. These measurements were acquired in the Mid-Atlantic Bight in September 2019 (Fig. 2 and Table 1). The first radiometric system (s/n: MPR-184) was operated by the UMB team, while the second one (s/n: MPR-179) was deployed at the same time by the team from the NOAA Center for Satellite Applications and Research (STAR). The two packages shared the same configuration and the same types of radiometers, and were calibrated with the same sources at STAR before the cruise. They were deployed side-by-side in the field and collected the radiance and irradiance data almost simultaneously.

For data processing, we adopted largely the same procedures as detailed in Section 3.2, specifically including: (i) *pre-processing*; (ii) *quality control of $L_w{}'(t)$ measurements*; (iii) *median spectra*; (iv) *correction for self-shading error*; and (v) *constraining the variability of*

Optics EXPRESS

incident irradiance. Note that, for Step (iii), only one median spectrum was determined for each deployment as the data segmentation is not necessary for the purpose of intercomparison. A total of 17 collocated measurements were obtained which span the optical water types from OWTs 1 to 15. CHL concentrations and bio-optical properties are moderate, with mean CHL of about 0.27 mg m^{-3}, and mean $a_{pg}(443)$ and $b_{bp}(443)$ equal to ~0.072 m^{-1} and ~0.0021 m^{-1}, respectively. All of these measurements were completed under mostly sunny skies, with the solar-zenith angle varying between 34° and 69°. The sea status was relatively calm during the field experiment.

Three metrics were used to quantify the differences between collocated radiometric data: the absolute unbiased percentage difference (UPD), bias, and root-mean-square difference (RMSD). They are specifically defined as below

$$UPD = median\left\{2 \times \sum_{i=1}^{N} \left|\frac{S_{1,i} - S_{2,i}}{S_{1,i} + S_{2,i}}\right|\right\} \times 100\%, \tag{13}$$

$$bias = median\left\{\sum_{i=1}^{N} \frac{S_{1,i} - S_{2,i}}{S_{2,i}}\right\} \times 100\%, \quad \text{and} \tag{14}$$

$$RMSD = \left[\frac{1}{N}\sum_{i=1}^{N} (S_{1,i} - S_{2,i})^2\right]^{1/2}, \tag{15}$$

where S_1 and S_2 refer to the radiometric quantities determined by STAR and UMB, respectively, and N is the total number of data points for comparison.

4. Results

4.1. Measurement precision of in situ radiance and reflectance

We first characterize the variability of in situ L_w and R_{rs} data. In Fig. 3, L_w and R_{rs} spectra are depicted in color in accordance with their OWTs. The values of R_{rs} and L_w vary over three orders of magnitude between 360–800 nm. No negative reflectance or radiance values are obtained at the ultraviolet (UV), blue, red, or near-infrared (NIR) bands. The non-zero observations can be partially ascribed to the virtue of direct sampling of radiance from the on-water approach (e.g., Eq. (3)). Still, L_w shares some important features with R_{rs}, particularly for the occurrences and locations of the spectral maxima and minima. The spectral variability and similarity of L_w and R_{rs} warrants the use of the optical classification scheme for a detailed quantification of their uncertainties.

In the following, we characterize the estimated precision for L_w in Fig. 4(a) and for R_{rs} data in Fig. 4(b). The uncertainties in Table 2 refer to spectrally averaged values of measurement precision for L_w and R_{rs}.

First, the values of U_{Lw} and U_{Rrs} at the UV and visible bands are conspicuously small, and they appear to be independent of the optical water types. An anomaly exists in OWT 22, in which L_w and R_{rs} are subjective to increased uncertainties. We found that the in situ data clustered in these types of waters represent those from turbid and highly absorptive waters. According to the estimation of the spectral absorption coefficient and CDOM and detritus absorption coefficient (a_{dg}), the a_{pg} values are 2.2, 1.4, 0.76, 0.31, 0.25 m^{-1} at 410, 443, 486, 551, and 671 nm, respectively, and the corresponding mean a_{dg} values are 1.7, 1.0, 0.47, 0.16, and 0.02 m^{-1}, respectively. Due to extremely high absorption coefficient, the resulting spectral R_{rs} values are very small. For example, the minimum and maximum spectral R_{rs} values, $R_{rs}(410)$ and $R_{rs}(551)$, are approximately 0.0017 and 0.0046 sr^{-1}, respectively. In addition, half of these measurements falling into OWT 22 were measured under cloudy to overcast skies, where their $E_s(410)$ values are only 1.5–50 μW cm^{-2} nm^{-1}. This represents an exceptional condition, under which the ocean color satellites often cannot have ocean color measurements.

Optics EXPRESS

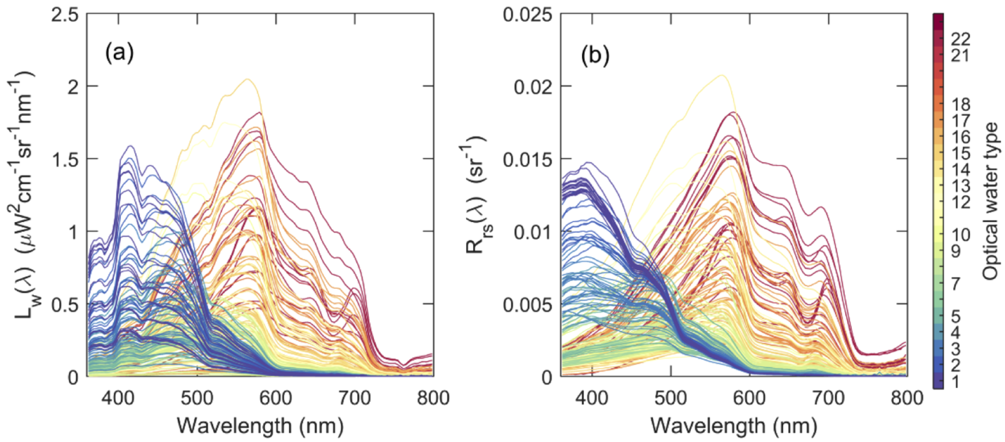

Fig. 3. Hyperspectral measurements in the coastal ocean for (a) water-leaving radiance L_w and (b) remote sensing reflectance R_{rs}. Note that only 17 labels are marked for the color bar in (b) to highlight the water types covered by this dataset. The complete classification scheme is described in Fig. 1(a).

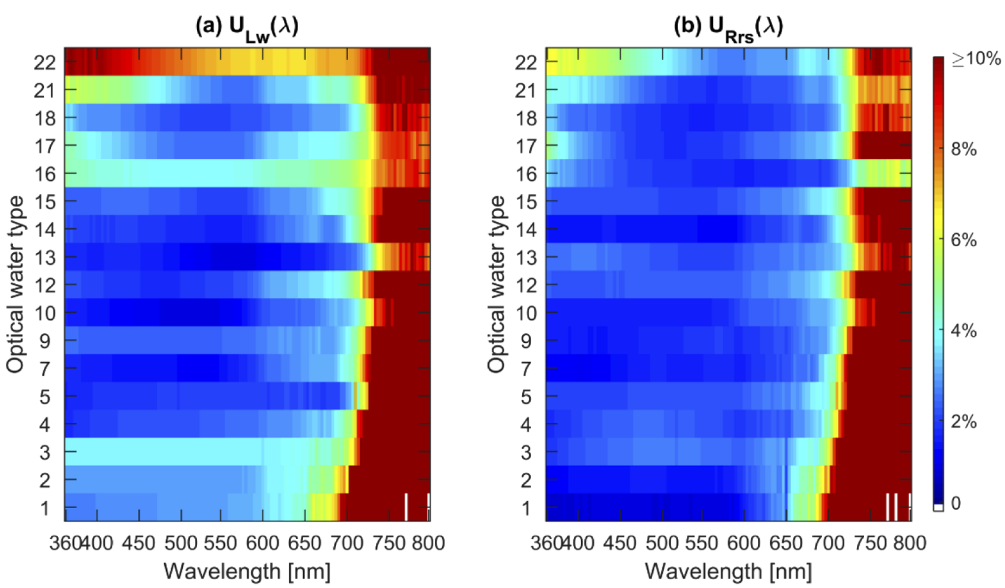

Fig. 4. Measurement precision for the on-water hyperspectral radiometric measurements of (a) radiance and (b) reflectance. The results are depicted with regard to the optical water types [33]; a total of 17 types are covered in our data.

Second, it is interesting to observe that U_{Rrs} is overall smaller than U_{Lw}, which is somewhat counterintuitive. From OWTs 1 to 21, specifically, U_{Lw} varies between ~1.5% and ~4.6%; U_{Rrs} varies between ~0.9% and ~4.4%. Such an observation is nevertheless possible, considering the following facts. On the one hand, these uncertainties are quantified based on the in situ measurements of L_w and E_s. As shown in Table 2, the CV's of $E_s(551)$ are around 6%, a value generally greater than reported E_s measurement uncertainties [30,31]. As such, these CV's may be ascribed to both the E_s measurement uncertainties and the variance of possibly non-stable incident irradiance itself. The latter can eventually propagate to L_w estimates, which would

Optics EXPRESS

Table 2. Measurement precision of in situ radiance and reflectance with respect to optical water types. The values given here represent spectrally averaged values. Note that fewer measurements were used for the quantification of U_{Lw} because of the data filtering for which the CV of the corresponding $E_s$data was less than 10%.

OWT	U_{Lw}				U_{Rrs}				CV(E_s) [a]
	360–600 nm	600–700 nm	700–800 nm	N	360–600 nm	600–700 nm	700–800 nm	N	
22	8.2%	7.0%	9.9%	6	4.4%	3.2%	7.8%	9	6.7%
21	3.9%	3.8%	8.7%	2	2.7%	2.5%	6.3%	3	5.7%
18	2.4%	2.7%	7.6%	3	2.1%	2.1%	7.0%	3	4.6%
17	3.0%	3.7%	7.2%	9	2.4%	2.8%	9.2%	22	4.4%
16	4.1%	4.6%	7.4%	5	2.2%	1.8%	4.6%	6	6.7%
15	2.3%	3.2%	9.5%	22	2.2%	3.0%	9.5%	30	4.4%
14	1.8%	2.8%	9.5%	5	1.4%	2.2%	8.3%	6	5.8%
13	1.4%	1.6%	6.4%	3	2.3%	2.7%	7.3%	4	5.4%
12	2.0%	3.5%	13.1%	15	2.3%	3.0%	12.3%	19	5.1%
10	1.3%	2.6%	8.9%	11	1.6%	2.6%	8.8%	12	4.7%
9	2.4%	3.0%	14%	21	1.7%	2.4%	14.1%	30	6.0%
7	1.5%	3.0%	17%	9	1.5%	2.4%	23.2%	14	5.2%
5	1.9%	2.1%	19%	5	2.1%	3.0%	21.3%	9	5.7%
4	2.2%	3.3%	26%	7	2.2%	2.7%	30.7%	13	5.1%
3	3.7%	4.2%	31%	11	2.4%	3.4%	47.4%	20	7.0%
2	3.0%	4.6%	49%	8	1.5%	3.8%	75.3%	12	6.7%
1	2.9%	5.4%	204%	17	0.9%	4.1%	48.7%	20	4.1%
Mean	2.7%	3.7%	36%	-	1.9%	2.8%	21%	232	-

[a]Mean of the coefficient of variation of $E_s(551)$.

increase the values of U_{Lw}. On the other hand, R_{rs} is the ratio of L_w to E_s, which covary, and therefore is largely insensitive to the change of instantaneous E_s. Therefore, U_{Rrs} is determined by the uncertainties from both L_w and E_s measurements. As a result, we may conclude that the values of U_{Lw} in Fig. 4(a) and Table 2 have likely been overestimated as some of the variation can be attributed to variation in ambient light field, rather to the ability to measure L_w.

Third, both U_{Lw} and U_{Rrs} show much larger values at the NIR bands than those at the UV and visible bands. Such a different performance is related to the small values of L_w and R_{rs} at the NIR bands. Besides, unlike the results at the UV-visible domain, U_{Lw}(NIR) and U_{Rrs}(NIR) demonstrate a dependency on OWTs. As shown in Table 2, they tend to decrease from the clearest waters (OWT 1 in this case) towards more turbid waters (OWT 22). Yet, the U_{Lw}(NIR) and U_{Rrs}(NIR) values of $>10\%$ are mostly found for OWTs from 1–9, where the magnitudes of L_w and R_{rs} are often much smaller than other types of waters.

Summarizing the uncertainty analyses, U_{Lw} is about 2.7% on average between 360 and 600 nm and 3.7% over 600–700 nm. U_{Rrs} is 1.9% over 360–600 nm and 2.8% for 600–700 nm. In the NIR bands, U_{Lw} and U_{Rrs} increase to significantly higher levels of 36% and 21%, respectively. We also note that the self-shading errors for each segmented data sequences of $\bar{L}_{w,i}$ and $\bar{R}'_{rs,i}$ could be infinitesimally close to each other. Ignoring the shading correction, we find that the derived uncertainties will reduce to ~1.9–2.3% for L_w and to ~1.5–1.8% for R_{rs} in the UV-visible domain.

Optics EXPRESS

4.2. Intercomparison of collocated measurements

For a clear presentation, we introduce notations of “STAR” and “UMB” to differentiate the collocated radiometric measurements.

Figure 5 first compares two sets of radiance data, denoted as L_w^{STAR} and L_w^{UMB}. For the purpose of simplicity, the comparisons only considered a few selected wavelengths. The error bars represent STD of the radiance measurements from each deployment, which are primarily a result of the variability of incident irradiance and sea surface waves. According to the comparisons, it is obvious that the two sets of L_w measurements agree with each other very well in the UV-visible domain. The spectrally averaged UPD is 3.4% with a near-zero bias and small RMSD of 0.0054 μW cm^{-2} sr^{-1} nm^{-1} (Fig. 5(a)). These small differences echo the high precision of radiance measurements identified in the previous section. In the NIR domain, much elevated differences are observable between L_w^{STAR} and L_w^{UMB}, where UPD = 26%, bias = 5.3%, and RMSD = 0.00096 μW cm^{-2} sr^{-1} nm^{-1} (Fig. 5(b)). The relatively larger differences can be explained partly by the small values of radiance at the NIR domain, which vary between ~0.001–0.01 μW cm^{-2} sr^{-1} nm^{-1}. Overall, the UPDs between L_w^{STAR} and L_w^{UMB} are comparable to the uncertainties of L_w measured with a single instrument given in Table 2 and Fig. 4.

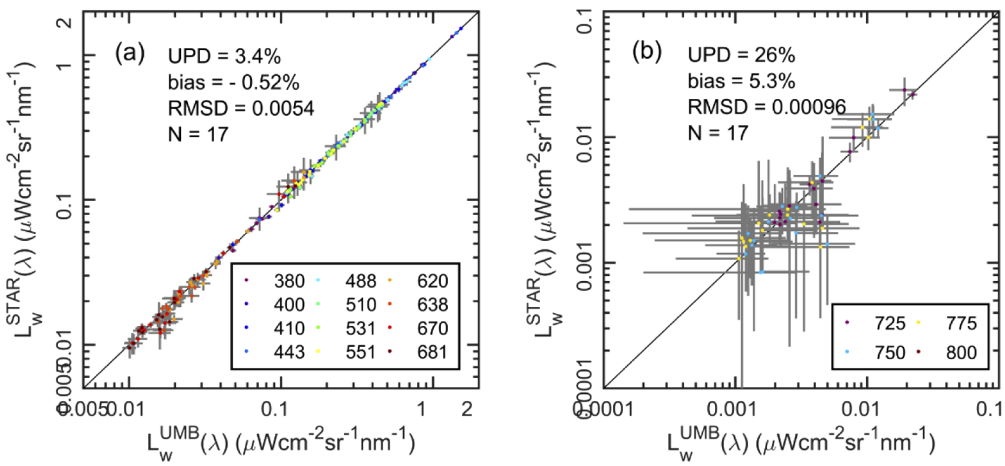

Fig. 5. Comparison of in situ water-leaving radiance from the collocated on-water radiometric measurements (differentiated with superscripts of “STAR” and “UMB”) for (a) the UV-visible bands and (b) NIR bands. The spectrally averaged UPD, bias, and RMSD are given in each plot, with the solid line representing 1:1. The colors are indicative of different wavelengths (see legend for details). The error bar refers to STD of each measurement.

We further compare the collocated R_{rs} data in Fig. 6. It is found that the two sets of R_{rs} measurements, R_{rs}^{STAR} and R_{rs}^{UMB}, are subjected to larger differences than those of L_w, where UPD = 8.6% at the UV-visible domain and UPD = 30% at the NIR bands. In addition, R_{rs}^{STAR} is generally higher by ~6.6% than R_{rs}^{UMB} at the UV-visible domain and by ~15% at the NIR bands. The differences between collocated R_{rs} products are expectedly greater than the radiances, partly because the R_{rs} data have involved irradiance measurements from two independent instruments. Indeed, we found that these elevated differences and biases at least partially can be traced back to the irradiance measurements. As shown in Fig. 7, the two sets of irradiance measurements, E_s^{STAR} and E_s^{UMB}, suffer larger differences, where UPD = 7.3% at the UV-visible domain and UPD = 9.2% at the NIR bands. In particular, E_s^{STAR} is generally lower compared to E_s^{UMB} by 5.8% at the UV-visible domain and by 6.5% at the NIR bands. Underestimation (or overestimation) of E_s can cause overestimation (or underestimation) of R_{rs}.

Optics EXPRESS

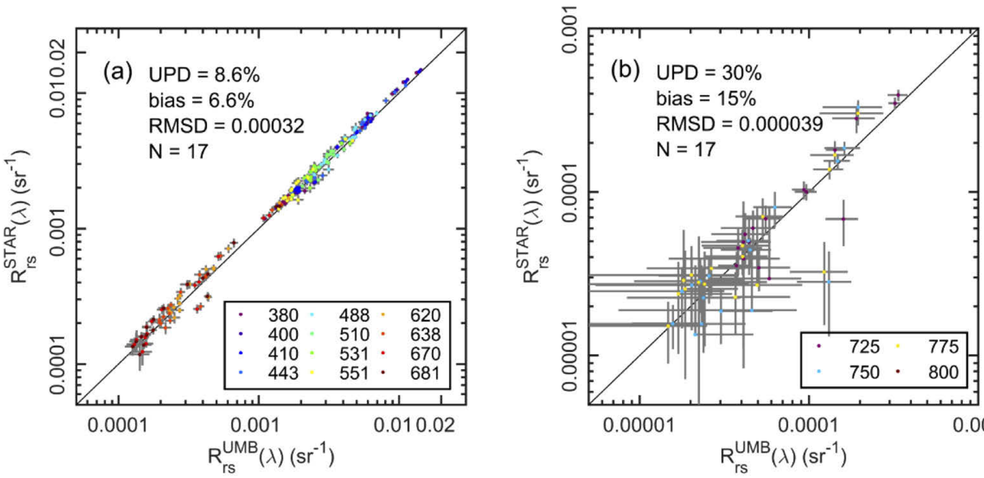

Fig. 6. Comparison of remote sensing reflectance derived from the collocated on-water radiometric measurements (differentiated with superscripts of "STAR" and "UMB") for (a) the UV-visible bands and (b) NIR bands.

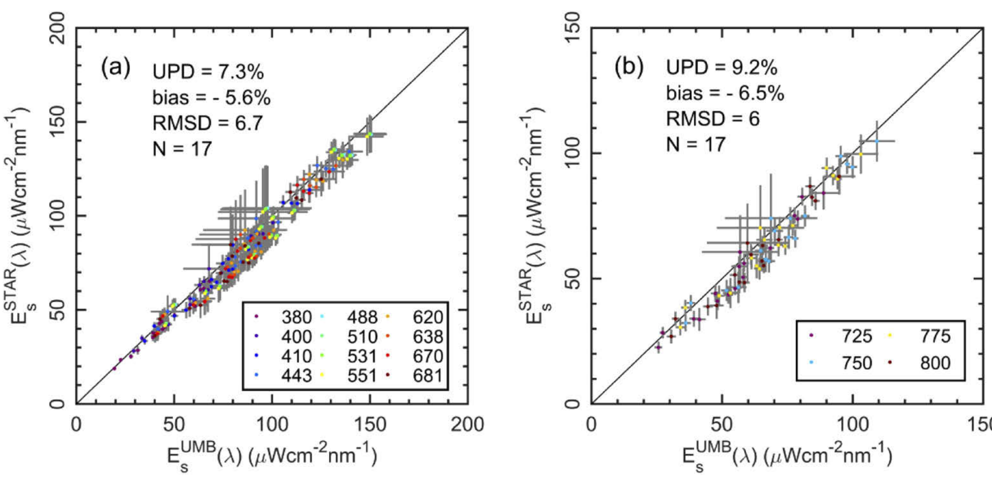

Fig. 7. Comparison of above-water downwelling irradiance from the collocated on-water radiometric measurements (differentiated with superscripts of "STAR" and "UMB") for (a) the UV-visible bands and (b) NIR bands.

In Fig. 8(a), we sorted the collocated radiance measurements into OWTs and then derived the UPD's for radiances within each of the OWTs. The classified UPD's show no dependency on OWTs at the UV and visible domain (also see Table 3 for the spectrally averaged UPD's). For wavelengths shorter than 600 nm, the UPD's of L_w^{STAR} and L_w^{UMB} are largely within ~3% (varying between 0.7% and 4.5%). This independence of OWTs agrees with the uncertainty results in Fig. 4(a). For the NIR bands, the UPD's are much larger, which in part is related to the small radiance values in this spectral range. Besides, the UPD's tend to decrease from OWT 1 toward OWT 8. An exception is with the radiance measurements in OWT 5, where the differences slightly increased but are still within ~10% for 600–700 nm. This increase of differences in OWT 5 is found related to one measurement obtained off of the east New Jersey coast; it is not clear yet of the underlying cause.

Optics EXPRESS

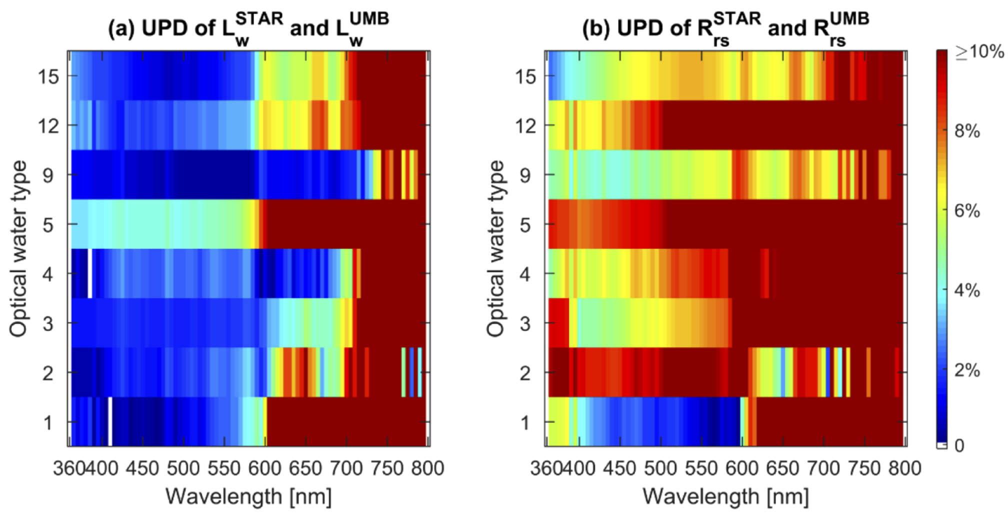

Fig. 8. Unbiased percentage difference of collocated on-water hyperspectral radiometric measurements for (a) radiance and (b) reflectance. The y-axis depicts the optical water types corresponding to the in situ measurements. White blanks represent no data available.

Table 3. Difference between the collocated measurement pairs with respect to optical water types. The values given here represent spectrally averaged values. The measurements are only considered for uncertainty analysis when $E_s$data are subject to variation with CV less than 10%.

OWT	UPD_{Lw}				UPD_{Rrs}			
	360-600 nm	600-700 nm	700-800 nm	N	360-600 nm	600-700 nm	700-800 nm	N
8	1.8%	6.0%	12.0%	2	5.8%	6.8%	10.1%	2
7	2.7%	6.9%	17.7%	1	9.1%	17.2%	23.5%	1
6	0.7%	1.2%	6.2%	2	5.2%	6.8%	8.3%	2
5	4.5%	12.3%	34.5%	3	9.6%	18.7%	40.8%	3
4	2.0%	2.0%	16.0%	2	7.3%	12.2%	25.1%	2
3	1.7%	4.4%	22.0%	4	6.7%	12.7%	29.9%	4
2	1.8%	6.3%	22.0%	2	9.5%	7.3%	20.6%	2
1	1.5%	18.3%	59.5%	1	2.4%	15.3%	62.8%	1
Mean	2.2%	6.5%	22.4%	–	7.2%	12.1%	26.8%	–

The OWT-specific comparison results for R_{rs} are given in Fig. 8(b) and Table 3. Most of the R_{rs} determinations show differences of well above 5%, partly due to differences in irradiance measurements. No persuasive dependencies are observed for the visible bands. Yet, the differences at the NIR bands decrease from OWTs 1 to 8.

It is worthwhile to discuss further the large differences between two irradiance measurements. We calibrated the radiometers before the field experiments following the standard ocean optics protocol. The overall differences between the lab-measured quantities and the light references are within ~0.5%. The sea state was relatively calm for these observations; so potential contamination of E_s measurements, for example, by possible sea sprays, cannot explain the rather systematic differences. One noticeable factor exists, however, that all of these field observations for intercomparison analysis were conducted under very large solar-zenith angles, with θ_s varying between 33° and 68° (the median solar-zenith angle is 57°) (Table 1). If there are differences in the cosine response between the two irradiance sensors, large differences (up to ~15%) may be

Optics EXPRESS

possible for E_s measurements under such large θ_s values [16,39]. More effort is certainly needed for a continued investigation into the potential errors associated with these irradiance sensors or irradiance sensors in general.

5. Discussion

5.1. Uncertainty components of the measurement results

The measurement precision of water-leaving radiance from the on-water approach is composed of two contributors: the uncorrected radiance $L_w{}'$ and the self-shading error ε. From the measurement equation of Eq. (3), U_{Lw} can be expressed as

$$U_{Lw}^2 = \left(\frac{\partial L_w}{\partial L_w{}'}\right)^2 U_{L_w{}'}^2 + \left(\frac{\partial L_w}{\partial \varepsilon}\right)^2 U_\varepsilon^2 + \Delta, \tag{16}$$

where $U_{Lw'}$ and U_ε represent the uncertainties for $L_w{}'$ and ε, respectively, and Δ represents the covariance term which involves the covariance between $L_w{}'$ and ε, $\partial L_w/\partial L_w{}'$, and $\partial L_w/\partial\varepsilon$. The two partial derivative terms are readily determined from Eq. (3), with $\partial L_w/\partial L_w{}' = 1/(1-\varepsilon)$ and $\partial L_w/\partial\varepsilon = L_w{}'/(1-\varepsilon)^2$. Together, it is U_ε, $U_{Lw'}$, and the values of ε and $L_w{}'$ that affect the measurement uncertainty of L_w.

The shadowing correction was performed with a model specifically designed for the systems equipped with the skylight-blocking apparatus [35]. The model requires the intermediate reflectance spectrum, i.e., $\bar{R}'_{rs,i}$, which is the median spectrum for each individual segment of data sequence in Section 3.2. Uncertainties associated with $\bar{R}'_{rs,i}$ will transfer to ε_i during the spectral estimation, which further propagate to the final products of L_w and R_{rs}. To understand the roles of the shading correction, we estimated U_ε by following the same procedures described in Section 3.2. In Table 4, the spectrally averaged U_ε values are given for each of their OWTs. First, the results clearly show that U_ε is dependent on the water types. Specifically, as suggested in Table 4, U_ε increases from OWTs 1 to 22. In other words, it decreases with the blue-green R_{rs} ratios, $R_{rs}(443)/R_{rs}(551)$, or equivalently, increases with CHL. Still, the maximum values of U_ε are shown to be within 3.4%, 1.21%, and 0.31% for the spectral ranges of 360–600 nm, 600–700 nm, and 700–800 nm, respectively. Such dependencies reflect the sensitivity of shading errors to the estimation of absorption and backscattering coefficients in Eq. (8) [35]. Second, it is evident that U_ε is spectrally dependent; it decreases from the UV bands toward longer wavelengths. On average, U_ε is ~2% over 360–600 nm, ~0.3% for 600–700 nm, and only ~0.05% at the NIR bands for the waters in this study. Such a dependency, at least partially, is related to the fact that the pure seawater absorption and scattering coefficients play a relatively bigger role in determining the estimation of ε at the NIR bands.

The $L_w{}'$ measurements obtained as such are liable to the influence of the sea surface waves. The sea waves induce the in-water light field fluctuations [40], which then propagate to the upwelling radiance L_u [41]. With the above-estimated U_ε, we derived $U_{Lw'}$ from Eq. (16) by assuming negligible contribution of Δ. Note that, because of this assumption, the values given in Table 4 best describe the upper limits of $U_{Lw'}$. According to the tabulated results, $U_{Lw'}$ is spectrally dependent, increasing towards longer wavelengths, which is opposite to U_ε. On average, $U_{Lw'}$ is ~2.2% over 360–600 nm, ~3.5% for 600–700 nm, and ~29% for 700–800 nm. Such spectral variation could primarily be a result of the spectral dependence of the light field [40]. In addition, results in Table 4 exhibit weak covariation of $U_{Lw'}$ with the OWTs, where the surface waves might have complicated this dependency.

To sum up, $U_{Lw'}$ is generally greater than U_ε over the full spectral domain between 360 and 800 nm. As $\partial L_w/\partial L_w{}'$ is usually greater than $\partial L_w/\partial\varepsilon$, it can be deduced that $U_{Lw'}$ will play a larger role in determining the measurement precision of L_w.

Optics EXPRESS

Table 4. Comparison of the uncertainty for estimated self-shading error and measured radiance (U_ε and $U_{Lw'}$) in different water types.

OWT	U_ε			$U_{Lw'}$			R_{rs} (443/551)
	360–600 nm	600–700 nm	700–800 nm	360–600 nm	600–700 nm	700–800 nm	
22	3.4%	0.98%	0.31%	7.2%	6.5%	8.3%	0.28
21	1.3%	0.63%	0.10%	3.2%	3.5%	6.9%	0.29
18	1.5%	0.28%	0.06%	2.1%	2.6%	6.0%	0.34
17	2.0%	0.63%	0.15%	2.4%	3.5%	5.7%	0.40
16	2.3%	1.21%	0.28%	2.5%	3.9%	6.1%	0.41
15	2.7%	0.47%	0.04%	1.6%	3.1%	7.4%	0.48
14	1.5%	0.42%	0.07%	1.6%	2.6%	7.8%	0.48
13	1.6%	0.37%	0.02%	1.2%	1.6%	5.0%	0.56
12	2.6%	0.34%	0.04%	1.3%	3.3%	10%	0.63
10	2.1%	0.31%	0.02%	0.7%	2.5%	6.8%	0.78
9	1.8%	0.07%	0.01%	2.0%	2.9%	11%	0.92
7	2.7%	0.14%	0.01%	0.8%	2.8%	13%	1.2
5	2.5%	0.10%	0.01%	1.3%	2.0%	15%	1.8
4	0.62%	0.01%	0.003%	2.1%	3.1%	20%	2.6
3	0.52%	0.01%	0.005%	3.6%	4.0%	23%	3.5
2	0.69%	0.02%	0.01%	2.8%	4.4%	36%	5.5
1	0.60%	0.00%	0.00%	2.7%	5.1%	166%	6.0
Mean	1.9%	0.30%	0.05%	2.2%	3.5%	29%	–

5.2. Quality control of the uncorrected radiance $L_w{}'$

The quality control of the uncorrected radiance measurements $L_w{}'$ is essentially to use a filter to remove potentially contaminated data. We developed this data filtering procedure in accordance with the pattern of movement of the instrument. Sitting at the surface, for example, the instrument will likely move up and down with the passage of big waves. Consequently, the skylight-blocking cone may completely rise above the water surface, such that the unwanted ambient light (skylight and sunlight) can instantly reach the fore optics of the radiance sensor. As a result, such contaminated radiance will be greater than L_w. On the other hand, it is also possible for the cone to submerge such that the entrance window of the radiance sensor is completely immersed in water. The radiance measured by a submerged radiometer can be described as $L_w{}' = L_u{}' \cdot \exp[z \cdot K_L]$, where $L_u{}'$ is an "apparent" upwelling radiance at depth z. $L_u{}'$ is different from L_u because the radiance sensor is calibrated for "in-air" observation, and hence, assumes no immersion effect. In fact, $L_u{}'$ is equal to the true in-water radiance L_u at this specific depth divided by the immersion coefficient for seawater, i.e., $L_u{}' = L_u/I_f$, where I_f is the immersion factor. We know that the commercial radiance sensors such as the Satlantic radiometers usually have an immersion factor of around 1.7 [42]. In addition, the exponential term $\exp[z \cdot K_L]$ is only slightly above 1. For example, it is about 1.03 with an assumption of $z = 0.03$ m and $K_L = 1$ m^{-1}. It can be deduced that $L_u{}' \exp[z \cdot K_L]$ is about half of the upwelling radiance right below the water surface, $L_u(0^-)$. That is to say, the radiance measured by a submerged sensor is smaller than L_w. The above discussion regarding the wave-induced over- and under-estimation of L_w corroborates the use of step (ii) in Section 3.2 for the filtering of the instantaneously recorded radiance $L_w{}'$. The filtering process, the residual errors, and roughened sea surface together have contributed to $U_{Lw'}$.

From an experimentalist's point of view, under the most unfavorable wavy conditions, at least 1/3 of the continuous measurements are valid data. The current analysis assumed a moderate threshold (±15%) for data filtering. Constraining the threshold will not significantly affect the radiometric products. In Table 5, we provide comparisons of the water-leaving radiance products after applying different thresholds: ±30% and ±15%. As expected, the UPD's among L_w are generally within ~0.3% except for red and NIR bands where L_w have very small values. The biases and RMSD are negligibly small as well. To increase or relax the threshold will not significantly affect final products of L_w and R_{rs}.

Table 5. Differences between water-leaving radiance L_w derived with thresholds of ±30% and ±15% [a]

	380 nm	412 nm	443 nm	488 nm	551 nm	667 nm	715 nm
UPD	0.17%	0.15%	0.16%	0.16%	0.27%	1.4%	2.9
Bias	0.025%	0.032%	0.015%	−0.017%	−0.045%	−0.22%	−0.75%
RMSD	5.2×10^{-4}	9.8×10^{-4}	0.0012	0.0012	9×10^{-4}	8.6×10^{-4}	7.3×10^{-4}

[a] Results are based on the in situ measurements (N = 17) in the Mid-Atlantic Bight in September 2019.

5.3. Dependency on the water types

Previous studies often referred to the water types as either Case 1 or Case 2, which is a classification scheme proposed by Morel and Prieur [43]. We did not use this binary scheme in that the Case 1–Case 2 classification is an oversimplification of the optical properties, in particular, of the coastal ocean. This is obvious in view of the variable spectral shapes and magnitudes of reflectance spectra as indicated in Fig. 1(a). Instead, the optical water types in this study result from a hard classification [33], which can assign a specific OWT to given R_{rs} spectra.

The uncertainty results quantified for L_w and R_{rs} at the UV-visible domain show no sign of dependency on the OWTs. This observation underlines the reliability of the on-water radiometric measurements. Such results can be attributed to the distinctiveness of the on-water radiometry — it largely bypasses the surface correction in Eq. (1) and the extrapolation and transmission in Eq. (2). Similar to an in-water approach, the on-water measurements have to be corrected for the shading errors, which play a secondary role in the total precision of L_w (Table 4).

6. Conclusions

The calibration of in-orbit satellite ocean color sensors requires that the ground-truth data should be achieved within ∼1–2% uncertainties. Toward this goal, great efforts were invested to assess ground-truth measurement uncertainties, particularly from the in- and above-water approaches. In this study, we have focused on a relatively less studied method — the on-water radiometry. We specifically addressed the measurement precision problems associated with the water-leaving radiance measurements from this approach.

Our examination reveals that the measurement precision of L_w (for the data precision) from the on-water approach can reach satisfactorily high levels, with the upper limits at 2.7–3.7% on average, over the UV-visible spectral domain. In addition, we find that such low uncertainties are achievable across different optical water types. The low levels of radiance uncertainties and the independence of the optical water types are an important attribute to this new method. We also assessed the measurement precision of R_{rs} products, which is about 1.9% over 360–600 nm and 2.8% for 600–700 nm.

The intercomparison of the collocated measurements allow for further evaluation of the consistency in the field measurement of water-leaving radiance. In general, our analyses show that the collocated radiometric data are highly consistent with each other. The L_w data are only subjected to a difference of less than ∼3.4% over 360–600 nm. The corresponding R_{rs} data pairs suffer increased differences of up to ∼8.6% due to a difference originating from variable irradiance measurements.

Optics EXPRESS

According to these analyses and earlier results, precise measurements of water-leaving radiance are attainable from the on-water approach for a wide range of waters, including stratified or shallow bottom waters. These features are important for supporting satellite calibration as well as validation exercises.

Funding. The Joint Polar Satellite System (JPSS) funding; National Oceanic and Atmospheric Administration; National Aeronautics and Space Administration.

Acknowledgments. This study was supported by the Joint Polar Satellite System funding and the GEO-CAPE projects (NNX16AD38G; 80NSSC18K0509). We are grateful to the research staff and students at University of Massachusetts Boston for assistance in field data collection. We also thank two anonymous reviewers for their useful comments. The scientific results and conclusions, as well as any views or opinions expressed herein, are those of the author(s) and do not necessarily reflect those of NOAA or the Department of Commerce.

Disclosures. The authors declare no conflicts of interest.

References

1. S. B. Hooker, W. E. Esaias, G. C. Feldman, W. W. Gregg, and C. R. McClain, "An overview of SeaWiFS and ocean color," 10456 (NASA Goddard Space Flight Center, Greenbelt, MD, 1992).
2. IOCCG, *Minimum requirements for an operational, ocean-colour sensor for the open ocean* (International Ocean Colour Coordinating Group, Dartmouth, Canada, 1998), pp. 46.
3. IOCCG, *Mission requirements for future ocean-color sensors* (International Ocean Colour Coordinating Group, Dartmouth, Canada, 2012), Vol. 13, pp. 106.
4. G. Zibordi, F. Mélin, J. M. Voss, B. C. Johnson, B. A. Franz, E. J. Kwiatkowska, J.-P. Huot, M. Wang, and D. Antoine, "System vicarious calibration for ocean color climate change applications: requirements for in situ data," Remote Sens. Environ. **159**, 361–369 (2015).
5. S. W. Bailey, S. B. Hooker, D. Antoine, B. A. Franz, and P. J. Werdell, "Sources and assumptions for the vicarious calibration of ocean color satellite observations," Appl. Opt. **47**(12), 2035–2045 (2008).
6. M. Wang and H. R. Gordon, "Calibration of ocean color scanners: how much error is acceptable in the near infrared?" Remote Sens. Environ. **82**(2-3), 497–504 (2002).
7. M. Wang, W. Shi, L. Jiang, and K. Voss, "NIR- and SWIR-based on-orbit vicarious calibrations for satellite ocean color sensors," Opt. Express **24**(18), 20437–20453 (2016).
8. C. R. McClain, G. C. Feldman, and S. B. Hooker, "An overview of the SeaWiFS project and strategies for producing a climate research quality global ocean bio-optical time series," Deep-Sea Res. Pt. II **51**(1-3), 5–42 (2004).
9. T. Cui, Q. Song, J. Tang, and J. Zhang, "Spectral variability of sea surface skylight reflectance and its effect on ocean color," Opt. Express **21**(21), 24929–24941 (2013).
10. Z. P. Lee, Y.-H. Ahn, C. Mobley, and R. Arnone, "Removal of surface-reflected light for the measurement of remote-sensing reflectance from an above-surface platform," Opt. Express **18**(25), 26313–26342 (2010).
11. G. Zibordi, F. Mélin, J.-F. Berthon, B. Holben, I. Slutsker, D. Giles, D. D'Alimonte, D. Vandemark, H. Feng, G. Schuster, B. E. Fabbri, S. Kaitala, and J. Seppälä, "AERONET-OC: A network for the validation of ocean color primary products," J. Atmos. Ocean. Technol. **26**(8), 1634–1651 (2009).
12. J. Wei, Z. P. Lee, M. Lewis, N. Pahlevan, M. Ondrusek, and R. Armstrong, "Radiance transmittance measured at the ocean surface," Opt. Express **23**(9), 11826–11837 (2015).
13. K. J. Voss and S. Flora, "Spectral dependence of the seawater–air radiance transmission coefficient," J. Atmos. Ocean. Technol. **34**(6), 1203–1205 (2017).
14. H. R. Gordon and K. Ding, "Self-shading of in-water optical instruments," Limnol. Oceanogr. **37**(3), 491–500 (1992).
15. S. B. Hooker, G. Lazin, G. Zibordi, and S. McLean, "An evaluation of above- and in-water methods for determining water-leaving radiances," J. Atmos. Ocean. Technol. **19**(4), 486–515 (2002).
16. V. Vabson, J. Kuusk, I. Ansko, R. Vendt, K. Alikas, K. Ruddick, A. Ansper, M. Bresciani, H. Burmester, M. Costa, D. D'Alimonte, G. Dall'Olmo, B. Damiri, T. Dinter, C. Giardino, K. Kangro, M. Ligi, B. Paavel, G. Tilstone, R. Van Dommelen, S. Wiegmann, A. Bracher, C. Donlon, and T. Casal, "Field intercomparison of radiometers used for satellite validation in the 400–900 nm range," Remote Sens. **11**(9), 1129 (2019).
17. T. Harmel, A. Gilerson, S. Hlaing, A. Tonizzo, T. Legbandt, A. Weidemann, R. Arnone, and S. Ahmed, "Long Island Sound Coastal Observatory: Assessment of above-water radiometric measurement uncertainties using collocated multi and hyperspectral systems," Appl. Opt. **50**(30), 5842–5860 (2011).
18. K. G. Ruddick, K. Voss, E. Boss, A. Castagna, R. Frouin, A. Gilerson, M. Hieronymi, B. C. Johnson, J. Kuusk, Z. Lee, M. Ondrusek, V. Vabson, and R. Vendt, "A Review of Protocols for Fiducial Reference Measurements of Water-Leaving Radiance for Validation of Satellite Remote-Sensing Data over Water," Remote Sens. **11**(19), 2198 (2019).
19. D. K. Clark, M. A. Yarbrough, M. Feinholz, S. Flora, W. Broenkow, Y. S. Kim, B. C. Johnson, S. W. Brown, M. Yuen, and J. L. Mueller, "MOBY, a radiometric buoy for performance monitoring and vicarious calibration of satellite ocean color sensors: measurement and data analysis protocols," in *NASA Tech. Memo. 2004-211621* (NASA, Goddard Space Flight Center, Greenbelt, MD, 2003), pp. 138–170.

20. D. Antoine, F. d'Ortenzio, S. B. Hooker, G. Bécu, B. Gentili, D. Tailliez, and A. J. Scott, "Assessment of uncertainty in the ocean reflectance determined by three satellite ocean color sensors (MERIS, SeaWiFS and MODIS-A) at an offshore site in the Mediterranean Sea (BOUSSOLE project)," J. Geophys. Res. **113**, C07013 (2008).
21. Y.-H. Ahn, "Development of redtide and water turbidity algorithms using ocean color satellite," (KORDI Seoul, Korea, 1999).
22. Z. P. Lee, N. Pahlevan, Y.-H. Ahn, S. Greb, and D. O'Donnell, "Robust approach to directly measuring water-leaving radiance in the field," Appl. Opt. **52**(8), 1693–1701 (2013).
23. Z. P. Lee, J. Wei, Z. Shang, R. Garcia, H. M. Dierssen, J. Ishizaka, and A. Castagna, "On-water radiometry measurements: skylight-blocked approach and data processing," in *Appendix to Protocols for Satellite Ocean Colour Data Validation: In Situ Optical Radiometry. IOCCG Ocean Optics and Biogeochemistry Protocols for Satellite Ocean Colour Sensor Validation, Volume 3.0*, G. Zibordi, K. J. Voss, B. C. Johnson, and J. L. Mueller, eds. (IOCCG Dartmouth, NS, Canada, 2019), pp. 7.
24. A. Tanaka, H. Sasaki, and J. Ishizaka, "Alternative measuring method for water-leaving radiance using a radiance sensor with a domed cover," Opt. Express **14**(8), 3099–3105 (2006).
25. G. Zibordi and M. Talone, "On the equivalence of near-surface methods to determine the water-leaving radiance," Opt. Express **28**(3), 3200–3214 (2020).
26. J. Wei, Z. P. Lee, R. A. Garcia, M. L. Zoffoli, R. Armstrong, Z. Shang, P. Sheldon, and R. F. Chen, "An assessment of Landsat-8 atmospheric correction schemes and remote sensing reflectance products in coral reefs and coastal turbid waters," Remote Sens. Environ. **215**, 18–32 (2018).
27. X. Yu, Z. Lee, F. Shen, M. Wang, J. Wei, L. Jiang, and Z. Shang, "An empirical algorithm to seamlessly retrieve the concentration of suspended particulate matter from water color across ocean to turbid river mouths," Remote Sens. Environ. **235**, 111491 (2019).
28. M. Zhang, C. Hu, M. G. Kowalewski, S. J. Janz, Z. P. Lee, and J. Wei, "Atmospheric correction of hyperspectral airborne GCAS measurements over the Louisiana Shelf using a cloud shadow approach," Int. J. Remote Sens. **38**(4), 1162–1179 (2017).
29. L. Tian, S. Li, Y. Li, Z. Sun, Q. Song, and J. Zhao, "A floating optical buoy (FOBY) for direct measurement of water-leaving radiance based on the skylight-blocked approach (SBA): an experiment in Honghu Lake, China," J. Geophys. Res. **125**, e2020JC016322 (2020).
30. K. J. Voss, S. McLean, M. R. Lewis, C. Johnson, S. Flora, M. Feinholz, M. Yarbrough, C. C. Trees, M. S. Twardowski, and D. K. Clark, "An example crossover experiment for testing new vicarious calibration techniques for satellite ocean color radiometry," J. Atmos. Ocean. Technol. **27**(10), 1747–1759 (2010).
31. G. Zibordi, K. Ruddick, I. Ansko, G. Moore, S. Kratzer, J. Icely, and A. Reinart, "In situ determination of the remote sensing reflectance: an inter-comparison," Ocean Sci. **8**(4), 567–586 (2012).
32. T. S. Moore, J. W. Campbell, and H. Feng, "Characterizing the uncertainties in spectral remote sensing reflectance for SeaWiFS and MODIS-Aqua based on global in situ matchup data sets," Remote Sens. Environ. **159**, 14–27 (2015).
33. J. Wei, Z. P. Lee, and S. Shang, "A system to measure the data quality of spectral remote sensing reflectance of aquatic environments," J. Geophys. Res. **121**(11), 8189–8207 (2016).
34. J. Wei, X. Yu, Z. P. Lee, M. Wang, and L. Jiang, "Improving low-quality satellite remote sensing reflectance at blue bands over coastal and inland waters," Remote Sens. Environ. **250**, 112029 (2020).
35. Z. Shang, Z. P. Lee, Q. Dong, and J. Wei, "Self-shading associated with a skylight-blocked approach system for the measurement of water-leaving radiance and its correction," Appl. Opt. **56**(25), 7033–7040 (2017).
36. J. L. Mueller, G. S. Fargion, and C. R. McClain, "Radiometric measurements and data analysis protocols," NASA/TM-2003-21621/Rev-Vol III (NASA Goddard Space Flight Center, Greenbelt, MD, 2003).
37. Z. P. Lee, K. L. Carder, and R. Arnone, "Deriving inherent optical properties from water color: a multi-band quasi-analytical algorithm for optically deep waters," Appl. Opt. **41**(27), 5755–5772 (2002).
38. C. D. Mobley, "Estimation of the remote-sensing reflectance from above-surface measurements," Appl. Opt. **38**(36), 7442–7455 (1999).
39. S. Mekaoui and G. Zibordi, "Cosine error for a class of hyperspectral irradiance sensors," Metrologia **50**(3), 187–199 (2013).
40. J. Wei, M. R. Lewis, R. Van Dommelen, C. J. Zappa, and M. S. Twardowski, "Wave-induced light field fluctuations in measured irradiance depth profiles: A wavelet analysis," J. Geophys. Res. **119**(2), 1344–1364 (2014).
41. M. R. Lewis, J. Wei, R. van Dommelen, and K. J. Voss, "Quantitative estimation of the underwater radiance distribution," J. Geophys. Res. **116**(C7), C00H06 (2011).
42. G. Zibordi, "Immersion factor of in-water radiance sensors: assessment for a class of radiometers," J. Atmos. Ocean. Technol. **23**(2), 302–313 (2006).
43. A. Morel and L. Prieur, "Analysis of variations in ocean color," Limnol. Oceanogr. **22**(4), 709–722 (1977).